ISTITUTO NAZIONALE DI RICERCA METROLOGICA
Repository Istituzionale

Robust radiative cooling via surface phonon coupling-enhanced emissivity from SiO2 micropillar arrays

(Article begins on next page)

25 November 2024

Robust radiative cooling via surface phonon coupling-enhanced emissivity from SiO$_2$ micropillar arrays

Zhenmin Ding [a], Xin Li [a], Hulin Zhang [b], Dukang Yan [a], Jérémy Werlé [d], Ying Song [a], Lorenzo Pattelli [c,d,*], Jiupeng Zhao [a], Hongbo Xu [a,**], Yao Li [b,e,**]

[a] School of Chemistry and Chemical Engineering, Harbin Institute of Technology, Harbin 150001, PR China
[b] Center for Composite Materials and Structure, Harbin Institute of Technology, Harbin 150001, China
[c] Istituto Nazionale di Ricerca Metrologica (INRiM), Turin 10135, Italy
[d] European Laboratory for Non-Linear Spectroscopy (LENS), University of Florence, Sesto Fiorentino 50019, Italy
[e] Suzhou Laboratory, Suzhou, 215123, PR China

ARTICLE INFO

ABSTRACT

Silicon dioxide (SiO$_2$) is a prominent candidate for radiative cooling applications due to its low absorption in solar wavelengths (0.25–2.5 µm) and exceptional stability. However, its bulk phonon-polariton band results in a strong reflection peak in the atmospheric transparency window (8–13 µm), making it difficult to meet the requirements for sub-ambient passive radiative cooling. Herein, we demonstrate that SiO$_2$ micropillar arrays can effectively suppress infrared reflection at 8–13 µm and enhance the infrared emissivity by optimizing the micropillar array structure. We created a pattern with a height, spacing, and diameter of approximately 1.45 µm, 0.15 µm, and 0.35 µm, respectively, on top of a bulk SiO$_2$ substrate using reactive ion etching. The resulting surface phonon coupling of the micropillar array led to an increase in the thermal emissivity from 0.79 to 0.94. Outdoor tests show that the SiO$_2$ cooler with an optimized micropillar array can generate an average temperature drop of 5.5 °C throughout the daytime underneath an irradiance of 843.1 W m^{-2} at noon. Furthermore, the micropillar arrays endow the SiO$_2$ cooler with remarkable hydrophobic properties, attributed to the formation of F/C compounds introduced during the etching process. Finally, we also replicated the micropillar pattern onto the surface of industrial optical solar reflectors (OSRs), demonstrating similar emissivity and hydrophobicity enhancements. Our findings revealed an effective strategy for modifying the thermal management features of durable SiO$_2$ layers, which can be harnessed to cool OSRs and other similar sky-facing devices.

1. Introduction

Radiative cooling materials are a special class of materials characterized by a strong emissivity in the wavelength range of the atmospheric transparency window (8–13 µm) which allows them to dissipate their thermal energy directly into space and cool down to sub-ambient temperatures when exposed to the sky. As such, they hold promise for addressing the growing cooling needs exacerbated by global warming without requiring any electricity input [1–5] and are increasingly explored for water harvesting, nighttime thermoelectric generation, or cooling in concentrated solar plants [6–8]. Recently, polymer-based films have emerged as a widely researched class of materials for radiative cooling due to their excellent cooling properties and scalability for

practical applications [9]. However, many polymer-based materials present still limitations in terms of their UV stability or their environmental friendliness, which makes them less suitable for a number of applications in the building sector or for solar cell cooling. In contrast, SiO$_2$ radiative coolers are often used in very harsh conditions (including space applications), such as optical solar reflectors (OSRs), due to their ability to withstand UV radiation and extreme heat shocks [10]. Additionally, they possess superior flame resistance compared to most polymeric radiative cooling materials and pose no environmental or health concerns, unlike many commonly used fluorinated radiation-cooling polymers such as polytetrafluoroethylene (PTFE) or polyvinylidene fluoride (PVDF), which can wear out over time due to exposure to weathering agents and may release microplastics into the

environment [11–13]. For all these reasons, a universal ban on their use and production is currently under consideration in the EU, together with several other fluoropolymers [14].

For these reasons, SiO$_2$ is an attractive component in recent radiative coolers, in the form of either multilayer dielectric films, composite film fillers, or photonic structures [15–25]. For example, Raman et al. [26] originally prepared a radiative cooler with high reflection (97%) in the 400–2000 nm wavelength range and high emission in the mid-infrared band by growing alternating multilayer HfO$_2$ and SiO$_2$ films on a Si wafer substrate. Therein, sustained emissivity in the atmospheric window (8–13 μm) was achieved by means of the interference at thermal wavelengths by the alternating index contrast of layers deposited by electron beam evaporation. To upscale the fabrication of large-area radiative coolers, SiO$_2$ microparticles were usually embedded in polymer matrices, as first exemplified by Zhai et al. [27] with a silver-coated polymethylpentene film comprising randomly distributed SiO$_2$ microspheres, reaching an emissivity above 0.93 in the atmospheric window (8–13 μm) thanks to the broadening of the photon-polariton resonance at 9.7 μm obtained by high-order Fröhlich resonance in the microspheres. In both examples, the inclusion of controlled layers or microparticles of SiO$_2$ in a composite material improved its emissivity and overall cooling power but did not address the intrinsic emissivity limitation of pure SiO$_2$. To this end, researchers considered micro-structuring the surface of SiO$_2$ films based on theoretical simulations and micro-nano fabrication technologies. For instance, Whitworth et al. [28] showed the simulated results that SiO$_2$ microsphere arrays (microsphere period size > 6 μm) can enhance the emissivity of bulk SiO$_2$ by surface phonon polarization resonance. Zhu et al. [29] directly applied a photolithographic technique to prepare the SiO$_2$ photonic crystal layer with a period of 6 μm and a large etching depth of 10 μm on the surface of a silicon absorber, obtaining a near-uniform emissivity over the entire thermal wavelength range (2.5–25 μm), owing mainly to the index-matching effect of the tilted sidewalls of the deep photonic crystal holes. Moreover, Zhao et al [30]. also prepared a grating structure (1.4 μm width, 10 μm height, and 7 μm period), which increased the SiO$_2$ emissivity from 0.67 to 0.91, resulting in a temperature reduction of 3.6 °C compared with an unstructured photovoltaic cell. Despite the enhanced emissivity of these SiO$_2$ microstructured samples, their deep etching depth (>5 μm) and large periodic structure size (>3 μm) make them difficult and costly to fabricate, and may not be compatible with other devices such as optical solar reflectors (OSRs). A comparison of the different fabrication processes and associated costs is provided in Supplementary Note 5. In addition, current research on SiO$_2$ microstructured samples is often limited to either numerical-only or experimental-only studies, and even when both methods are employed, numerical simulations are simply used to replicate experimental results rather than to guide their improved design, which limits the performance of recently proposed microstructures on SiO$_2$ surfaces. In contrast, submicron structures are desirable due to their high compatibility with various manufacturing processes and their ability to enhance emissivity through impedance matching. Additionally, integrating theoretical simulations in the design process of the submicron pattern process will also facilitate the exploration of optimal parameters for submicron structures on SiO$_2$ surfaces [31]. Notably, this is not just relevant for radiative cooling applications, but also in other areas such as broadband solar absorbers for photothermal conversion [32,33].

In this work, we designed and fabricated optimized micropillar arrays on the surface of SiO$_2$ using finite-difference time-domain (FDTD) numerical simulations and the reactive ion etching (RIE) method. The simulation results have demonstrated the existence of an ideal range for the structural diameter of the micropillar, which falls within the range of 0.2–0.6 μm, accompanied by a spacing of 0.1–0.3 μm and a height of 1.4–2.2 μm. The cooler with an optimized micropillar array reveals an emissivity of 0.94 or higher in the 8–13 μm range and an average temperature drop of 5.5 °C throughout the daytime under an irradiance of 843.1 W m^{-2} at noon. Results of further electric field analysis reveal that

the highest electric field enhancement is observed in the wavelength of 9 μm, which is attributed to the phonon polarization resonance in the micropillar spacing. The above-submicron structure is found to be highly compatible with commercial optical solar reflectors (OSRs) and could effectively improve its emissivity and hydrophobicity. This approach is suitable for manipulating the thermal management characteristics of SiO$_2$ coatings for applications in cooling OSRs.

2. Experimental section

2.1. Materials

Bulk quartz (SiO$_2$) 40 × 40 × 1 mm^3 in size was purchased from Aladdin. Extra analytical grade reagents, including silver ingot particles (Ag), ethanol (C$_2$H$_5$OH), polystyrene spheres (PS), sodium dodecylbenzene sulfate (SDS), and acetone (CH$_3$COCH$_3$), were purchased from Tianjin Tianli Chemical Reagents Ltd. All gases used in the etching procedure, such as argon (Ar, 99.99%), nitrogen (N$_2$, 99.99%), and trifluoromethane (CHF$_3$, 99.99%), were obtained from Harbin Liming Gas Co., Ltd.

2.2. Preparation of SiO$_2$ microstructured surfaces with cylinder arrays

An ordered monolayer array mask of PS spheres is obtained by the self-assembly technique. The 400–600 nm PS spheres were added to a mixture of deionized water and ethanol with a volume ratio of 1:1 to obtain a 10% mass fraction solution. The above mixture was ultrasonicated for 30 min with a Fisherbrand model 505 sonic dismembrator. The bulk SiO$_2$ slides were ultrasonically washed in acetone, alcohol, and ultrapure water for 15 min each. Next, the wash is placed on the edge of the surface dish. The PS spheres slowly slide into a water-filled surface dish and self-assembled into a single-layer film. Finally, after 30 min of resting, the pre-washed SiO$_2$ sheet was gently lifted to collect the PS monolayer of spheres. The second step of this preparation process is the reactive ion etching process, which was carried out using an NRE-4000 system (Nano-Master, Inc, USA). After the etching process optimization was completed, PS spheres were treated in argon plasma for different times (10 min, 20 min, and 30 min). The parameters of the specific etching process are summarized in Table S4. Next, the above-processed sample was further subjected to reactive ion etching, with the platen bias (RF1) set to 50 W, and the inductively coupled plasma emission Spectrometer source (RF2) set to 150 W. The flow rates of CHF$_3$ and Ar were set to 20 and 12 sccm, respectively, and the pressure of the etching chamber was calibrated to 50 mtorr. The etching time was 30 min and started once the etching chamber reached a pressure below 4 × 10^{-5} mtorr. Next, the etched samples were washed in an acetone bath for 30 min to obtain a microstructured sample. The above-obtained samples were named sample 0 (0 min), sample 1 (5 min), sample 2 (10 min), and sample 3 (20 min) according to the Ar treatment time. Finally, the back (unstructured) side of each sample was coated with the deposition of 200 nm silver as a reflective layer. The deposition conditions are detailed in a previous study [31].

2.3. Characterization and measurements

The outdoor temperature measurement was carried out at Harbin Institute of Technology, Harbin City (45°74′N, 108°58′E) using a custom-made temperature measuring device on 12-13 July 2022. Scanning Electron Microscopy (SEM) (SIGMA 300, ZEISS, Germany) was used to measure the microscopic morphologies of all prepared samples. The solar spectral reflectance was determined by a UV-Vis-NIR spectrophotometer (Lambda-1050, Perkin Elmer, US) with a wavelength range of 0.25–2.5 μm. The infrared spectral reflectance of the samples in the wavelength from 2.5 to 25 μm was measured by an FT-IR spectrometer with an A562 integrating sphere. An IR thermal imager (Tix660, Fluke) was used to take thermal images of the samples with a

spectral range of 7.5–14 µm. The local solar irradiance was obtained by a solar power meter (TES-1333).

2.4. Cooling Power Calculations

As shown in Fig. S14, the cooler can reflect most of the sunlight and conduct high thermal power to outer space through the atmospheric window (8–13 µm) under a clear sky. At the same time, heat convection and conduction introduce thermal exchanges between the radiant cooler and the surrounding environment. Thus, non-radiative heat transfer should also be considered in the heat balance calculation. All heat exchange channels between the cooling film and the surrounding environment are presented in Fig. S14, and the related equations are shown in Eqs. (1)–(8) [5].

$$P_{net}(T) = P_{rad}(T) - P_{atm}(T_{amb}) - P_{sun} - P_{(cond+conv)} \tag{1}$$

where Eq. (1), P_{net} is the net cooling power of the cooler, and P_{rad} represents the thermal radiation power from the cooling surface in the 2.5–25 µm band. The total power emitted by a specific radiative cooler is expressed as

$$P_{rad}(T) = \int \cos\theta d\Omega \int_{2.5}^{25} \varepsilon(\lambda, \Omega) M_b(\lambda, T) d\lambda \tag{2}$$

$$M_b(\lambda, T) = \frac{C_1 \lambda^{-5}}{e^{C_2/\lambda T} - 1} \tag{3}$$

where T is the absolute temperature of the designed cooling surface. The integral: $\int d\Omega = \int_0^{\pi/2} \sin\theta d\theta$ is the angular integral for a hemisphere, θ is the local zenith angle, $\varepsilon(\lambda, \Omega)$ is the angle-dependent emissivity at wavelengths of 2.5–25 µm. $M_b(T, \lambda)$ is the black body spectral radiance intensity at temperature T, $M_b(T, \lambda)$ can be calculated by Eq. (3), where C_1 and C_2 are radiation constants valued 3.7418×10^8 W µm^4 m^{-2} and 1.4388×10^4 µm·K, respectively.

The weighted infrared emissivity in the infrared band (2.5–25 µm) can be calculated as:

$$\varepsilon_{2.5-25\mu m} = \frac{\int_{2.5\mu m}^{25\mu m} M_b(T, \lambda) \varepsilon(T, \Omega) d\lambda}{\int_{2.5\mu m}^{25\mu m} M_b(T, \Omega) d\lambda} \tag{4}$$

where $\varepsilon(T, \Omega)$ is the spectral emissivity of the cooler. According to Kirchhoff's law, the emissivity can be defined as: [29]

$$\varepsilon = 1 - R - T \tag{5}$$

where T is transmittance and R is the reflectance in IR spectroscopy.

P_{atm} (2.5–25 µm) is the power absorbed by incident atmospheric radiation:

$$P_{atm}(T_a) = \int d\Omega \cos\theta \int_{2.5}^{25} \varepsilon(\lambda, \Omega) \varepsilon_a(\lambda, \Omega) M_b(\lambda, T_a) d\lambda \tag{6}$$

The atmospheric emissivity is given by: $\varepsilon_a(\lambda, \Omega) = 1 - t(\lambda)^{1/\cos\theta}$, where $t(\lambda)$ is the atmospheric transmittance in the zenith direction [34, 35]. Besides, T_a is the ambient temperature (298.15 K).

P_{sun} (0.25–2.5 µm) is the incoming power absorbed from the sun:

$$P_{sun} = \int_{0.25}^{2.5} \varepsilon(\lambda, \theta_{sun}) E_{AM1.5}(\lambda) d\lambda \tag{7}$$

$E_{AM1.5}$, is the standard solar spectral irradiance received by AM1.5 ($\approx$893 W m^{-2}). θ_{sun} is the inclination of the radiation cooling device facing the Sun. The cooler's solar absorptivity ($\varepsilon(\lambda, \theta_{sun})$) is replaced with its absorptivity based on Kirchhoff's law.

h_{cc} represents the overall heat transfer coefficient used to evaluate the cooling loss power. Thus, the cooling loss power of the designed cooler can be summarized as.

$$P_{cond+conv} = h_{cc}(T_a - T) \tag{8}$$

Non-radiative heat transfer (i.e. conduction and convection) is described by $P_{cond+conv}$. For Eq. (6), T and T_a represent the cooler surface and ambient temperature (298.15 K), while the coefficient h_{cc} taken here is 0 W m^{-2} K^{-1}, 3 W m^{-2} K^{-1}, 6 W m^{-2} K^{-1}, 9 W m^{-2} K^{-1}, and 12 W m^{-2} K^{-1}, respectively.

3. Results and discussions

Fig. 1a reveals that pure flat SiO$_2$ has a pronounced reflectivity peak at approximately 9 µm. According to Kirchhoff's law [36], the emissivity of SiO$_2$ diminishes in this band, which has been corroborated by simulations and experiments. This is mainly caused by the surface phonon polarization excitons of the Si-O bond, and the underlying intrinsic reason is illustrated in Fig. S1 and Supplementary Note 1. To address this issue, a preliminary micropillar array diameter of 0.4 µm, spacing of 0.08 µm, and a height of 1.5 µm were realized on the surface of bulk SiO$_2$ to suppress infrared reflection at 8–13 µm (Fig. 1b). Simulation results demonstrate that this patterning strategy can lead to a significant emissivity increase (as seen in Fig. 1a and b), in good agreement with experimental results.

To further achieve the optimal structural parameters of the SiO$_2$ micropillar array, we performed FDTD simulations for an infinite periodic micropillar array on the SiO$_2$ surface. The detailed settings and structural parameters are shown in Fig. S2 and Supplementary Notes 2. The micropillar diameter of the hexagonal cylinder structure ranges from 0 to 1.0 µm, with a spacing of 0 to 0.3 µm and a height of 0–4.0 µm. High infrared emissivity levels are observed for the structural diameter of the micropillar within the range of 0.2–0.6 µm, with a spacing of 0.1–0.3 µm and a height of 1.4–2.2 µm, as depicted in Fig. 2a–f. It is evident that these three parameters are instrumental in regulating the duty cycle of the SiO$_2$ surface. As the structural parameters are adjusted, the coupling strength between the surface electromagnetic wave and the surface micropillar array alters, resulting in a different wavevector matching relationship between the incident electromagnetic wave and the SiO$_2$ medium, which in turn influences the phonon polarization resonance phenomenon, thus altering the emissivity of SiO$_2$ at 8–13 µm. Therefore, altering any of these three parameters can lead to significant emissivity variations. Even stronger dispersion can be observed beyond the sub-wavelength size range for the micropillar structure, with the onset of Mie-like resonances of the scattering elements. Upon analyzing the correlation between the structural parameters (diameter, spacing, height) of the micropillar and the infrared emissivity, the maximum infrared emissivity is obtained for micropillars with 0.4 µm in diameter, 0.2 µm in spacing, and 1.6 µm in height (Fig. S3). Additional simulations were also performed to determine the emissivity of an optimized SiO$_2$ with micropillar arrays with respect to the polarization angle. As shown in Fig. 2g, due to the sub-wavelength scale of the structure, the emissivity is largely insensitive to the incoming polarization at normal incidence. The data in Fig. 2h and i provide additional evidence that the optimized sample can sustain a high level of polarization-independent emissivity ($< 60°$) for both TE and TM polarizations.

Based on the outcome of our numerical simulation, the results of the initial optimization are shown in Fig. S4. All samples exhibited an increase in infrared emissivity, largely attributed to the presence of high micropillars on the SiO$_2$ surface guaranteeing a more gradual transition from the refractive index of air to that of the bulk SiO$_2$. An enhancement of the electric field is observed at both the touching point between the micropillars and along the edges, as illustrated in Fig. S5a and b, which confirms that arrays of contiguous micropillars can increase the emissivity of SiO$_2$. However, the infrared emissivity of all samples characterized by touching elements remains below 0.9, which is due to the vanishing gap between the micropillars, which are not spaced far
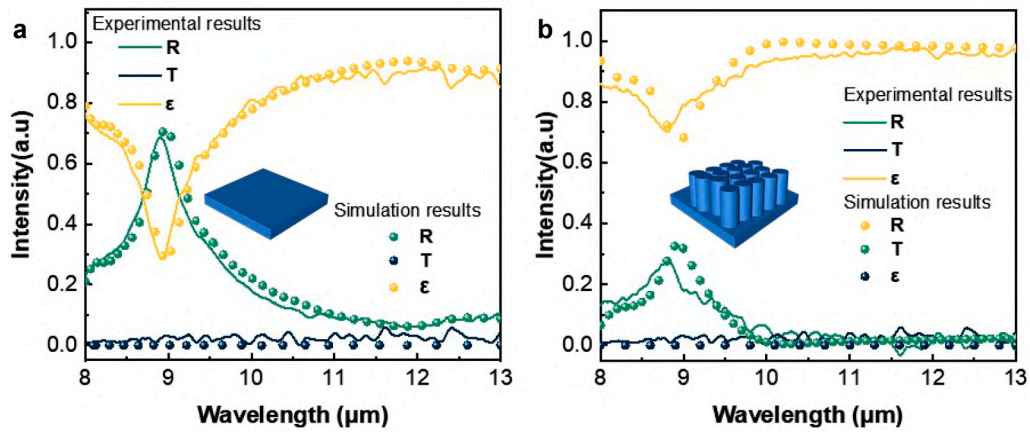
Fig. 1. (a) The simulated and experimental reflectivity (R), transmittance (T), and emissivity (ε) curves for the unpatterned (flat) SiO_2, and the inset is schematic diagrams for the flat SiO_2. (b) Simulated and experimental reflectivity (R), transmittance (T), and emissivity (ε) curves for the micropatterned SiO_2 emitter, respectively, and the inset is schematic diagrams for the SiO_2 with micropillar arrays.
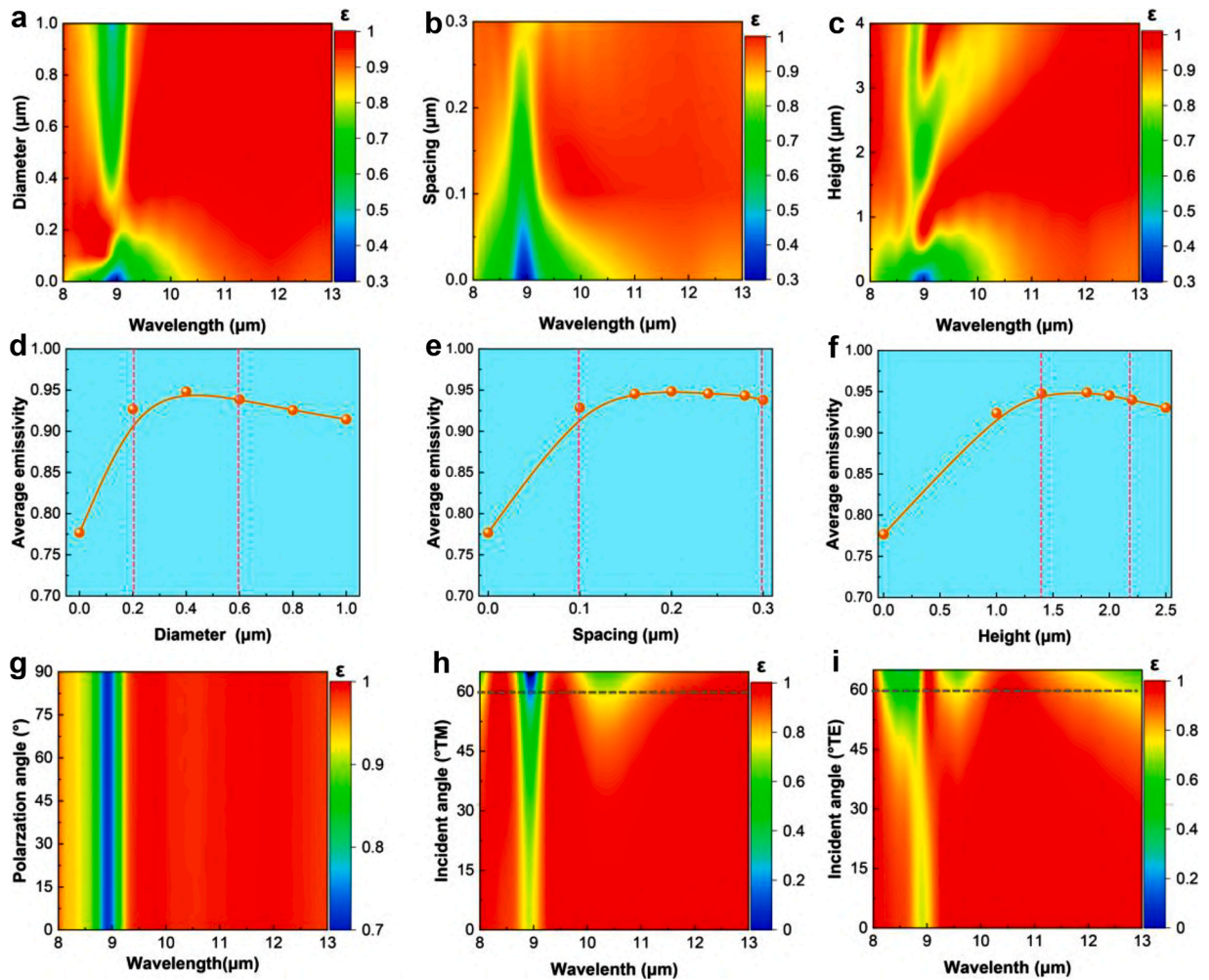

Fig. 2. FDTD simulation results of the SiO_2 with micropillar arrays in the wavelength of 8–13 μm. (a) Emissivity map *vs.* micropillar diameter, (b) Emissivity map *vs.* the spacing between micropillars, (c) Emissivity map *vs.* the height of micropillar. (d-f) show the corresponding infrared emissivity (8–13 μm) plots relative to micropillar diameter, the spacing between micropillars, and the height of the micropillar, respectively. (g) Emissivity dependence on polarization at normal incidence for the sample with micropillar diameter, spacing, and height of 0.2 μm, 0.4 μm, and 1.6 μm, respectively. (h–i) Angular dependence of the emissivity for transverse electric (TE) and transverse magnetic (TM) polarization.
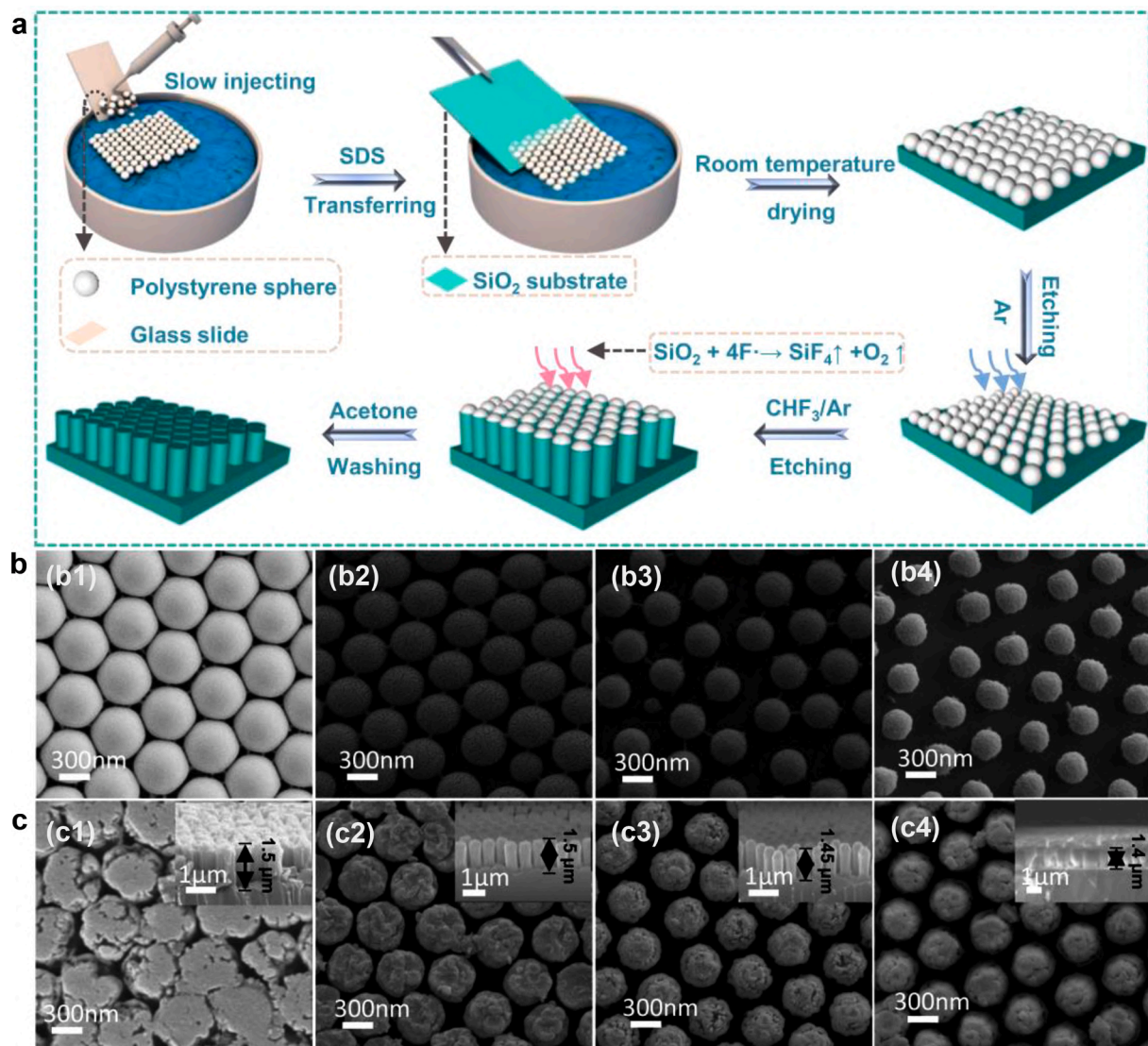
Fig. 3. (a) Schematic for the fabrication of the SiO_2 with the micropillar arrays on the surface (Sodium hexadecylbenzene sulfate (SDS)). (b) SEM images of the PS spheres with different Ar etching times: (b1) 0 min, (b2) 10 min, (b3) 15 min, (b4) 20 min. (c) Surface and cross-sectional SEM images (the insets) of the different samples (etching 30 min under CHF_3/Ar condition): (c1) sample 0, (c2) sample 1, (c3) sample 2, (c4) sample 3.

enough apart to form an effective phonon polariton resonance. Thus, the fabrication parameters were further tuned to match the optimized micropillar parameters according to the preparation steps summarized in Fig. 3a. The process involved the self-assembly of polystyrene (PS) spheres into a well-ordered monolayer on the surface of the water, which was later transferred onto a SiO_2 substrate. The resulting PS monolayers were subsequently exposed to argon (Ar) plasma treatment for varying durations in order to create controlled gaps between the spheres, which then served as etching masks. Consequently, the spacing size of the produced micropillars can be regulated accurately based on the duration of the Ar plasma preprocessing. The etching process involved the use of trifluoromethane (CHF_3) and argon (Ar) gases. The spacing between the spheres depicted in Fig. 3b has been observed to increase gradually over a period of 10–20 min, starting from 0.05 μm and reaching 0.15 μm at the 15 min and 0.2 μm at the 20 min. Correspondingly, the insets in Fig. 3c display the structure heights of the micropillar array after acetone washing, which measure approximately 1.5 μm, 1.5 μm, 1.45 μm, and 1.4 μm, respectively. Overall, we found that the structural parameters of the sample subjected to 15 minutes of Ar treatment align with the optimization range established in our prior numerical study.

Optical characterization of the different samples was performed, following the deposition of a 200 nm silver layer on the backside of each sample to serve as the reflective layer. Solar-weighted reflectance (0.25–2.5 μm) curves show no significant difference, averaging at about 95% for all three samples (Fig. S6a). The corresponding emissivity curves in the atmospheric transparency window (8–13 μm) are given in Fig. S6b, showing that sample 2 exhibits the highest integrated emissivity value (0.94), close to that obtained with numerical simulations (Fig. 4a). The emissivity enhancement can be highlighted via an infrared thermal imaging test by looking at different samples placed on an indoor hot plate, owing to the positive correlation between the apparent temperature of the sample surface and its emissivity [30]. Fig. 4b presents the IR thermal images of sample 2, in comparison to pure SiO_2 and a metallic aluminum sheet with low emissivity. It is evident that sample 2 has the highest apparent temperature and hence the highest emissivity, as compared to the bulk SiO_2 sample and the aluminum (Al) sheet. The electric field in the X-Z plane of a SiO_2 with micropillar arrays of varying structural parameters at a resonant wavelength of 8.9 μm is illustrated in Fig. 4c–e. When the spacing is 0.15 μm, the simulated electric field displays a significant enhancement, which is in agreement with the experimental results (Fig. 4a). Similarly, the results obtained at the
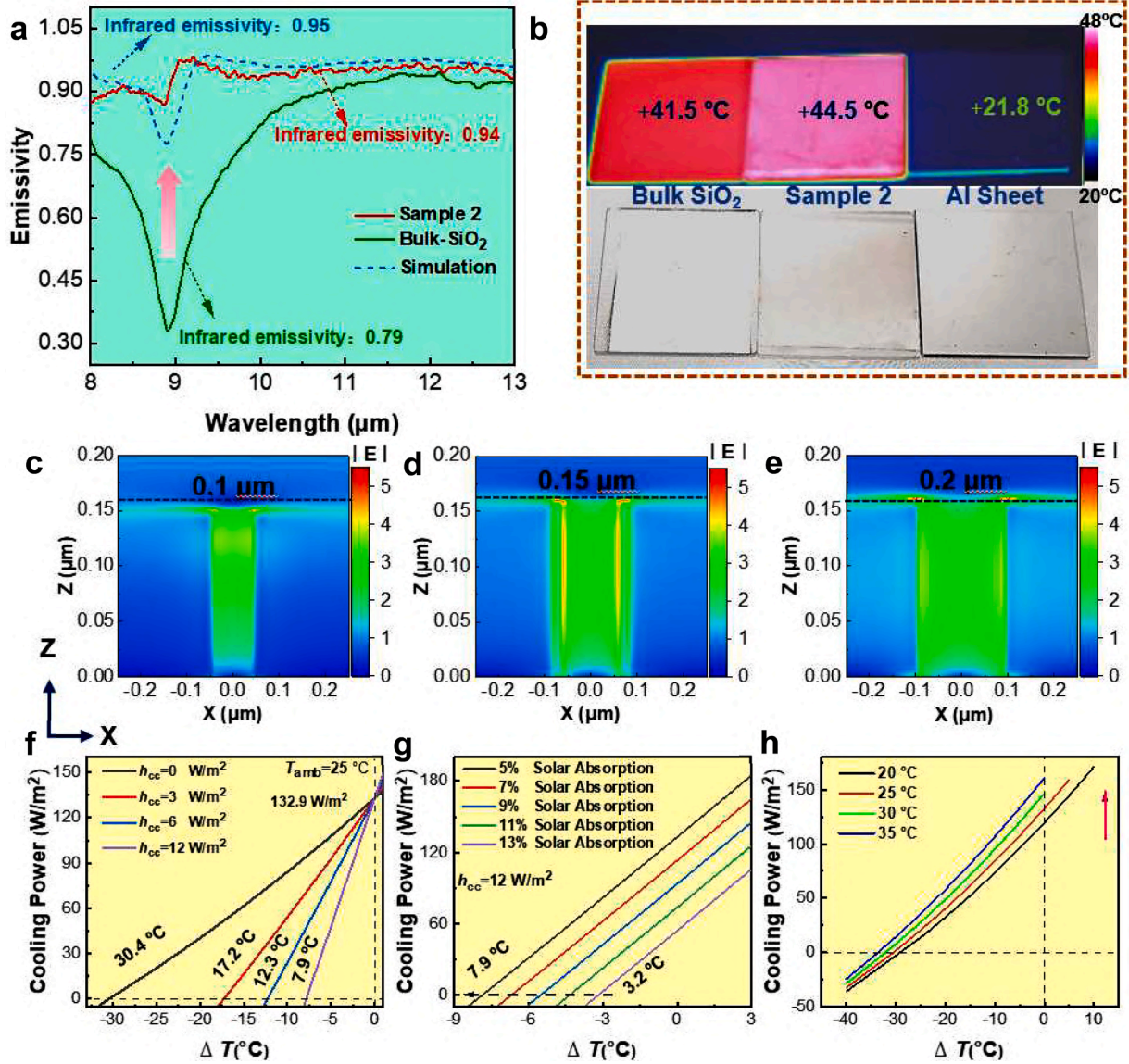
Fig. 4. (a) Measured emissivity of different samples in wavelength of 8–13 μm. (b) IR thermography of sample 2, Bulk SiO$_2$, and Al sheet at a testing temperature of 50 °C. The Y-component of the electric field in the X-Z plane with different spacing values at a wavelength of 8.9 μm: (c) 0.1 μm, (d) 0.15 μm, (e) 0.2 μm. (f) Predicted net cooling power at different non-radiative heat transfer coefficients (h_{cc}) of sample 2. (g) Predicted net cooling power at different solar absorption rates of sample 2. (h) Predicted net cooling power at different atmospheric temperatures of sample 2.

wavelengths of 9.1 μm and 9.3 μm (Fig. S7) demonstrate that the transverse photon resonance is efficiently coupled in the micropillar spacings, thereby enhancing the emissivity. Movie S1 describes the interaction of SiO$_2$ micropillar arrays in the Z-direction with IR light in the 8–13 μm band, which further confirms the existence of phonon resonance phenomena. The small spacings between the micropillars result in an increase in the intensity of the electric field, which is likely responsible for the formation of phonon polaritons that are coupled to free space similar to the surface plasmons that have been previously reported [37]. Using the spectral data of sample 2 presented in Fig. S8, the theoretical net cooling power of sample 2 can be calculated to be 136.4 W m^{-2} based on the AM1.5 solar spectral reference and the ambient temperature (T_a) of 298.15 K. The temperature reduction potential ranges from 7.9 to 30.5 °C when varying the non-radiative heat transfer coefficient between 12 and 0 W m^{-2} (Fig. 4f). Fig. 4g and h show how the cooling power is expected to decrease for larger values of solar absorption or to increase for higher ambient temperatures up to 35 °C, respectively.

In order to further examine the radiative cooling capabilities of

sample 2, outdoor cooling experiments were carried out from July 12th to 13th, 2022 on the rooftop of the Mingde Building at Harbin Institute of Technology. During this test period, the test data allows us to assess the radiative cooling effect of the designed cooler under different weather conditions, including particularly unfavorable conditions of very high relative humidity and cloudy sky. In this experiment, a custom-built apparatus was used to compare sample 2 and bulk SiO$_2$ (as a reference sample) under direct sunlight (Fig. 5a). A schematic diagram of the outdoor temperature measurement device is displayed in Fig. 5b, comprising foam walls wrapped in aluminum foil to protect the box from solar heat gains, and a clear polyethylene (PE) film to reduce heat convection fluctuations and decouple from variable external wind conditions [26]. Fig. 5c shows the local wind speed conditions and relative humidity (RH) (see Supplementary Note 4 and Fig. S9). On both days of measurement, the humidity was high, remaining above 50% on July 12 and above 80% on July 13 due to the cloudy weather, which is typical of the rainy season in northern China. This high humidity will have a negative effect on the potential cooling power of a passive radiative cooling material [38]. Solar irradiance was measured with a radiometer,
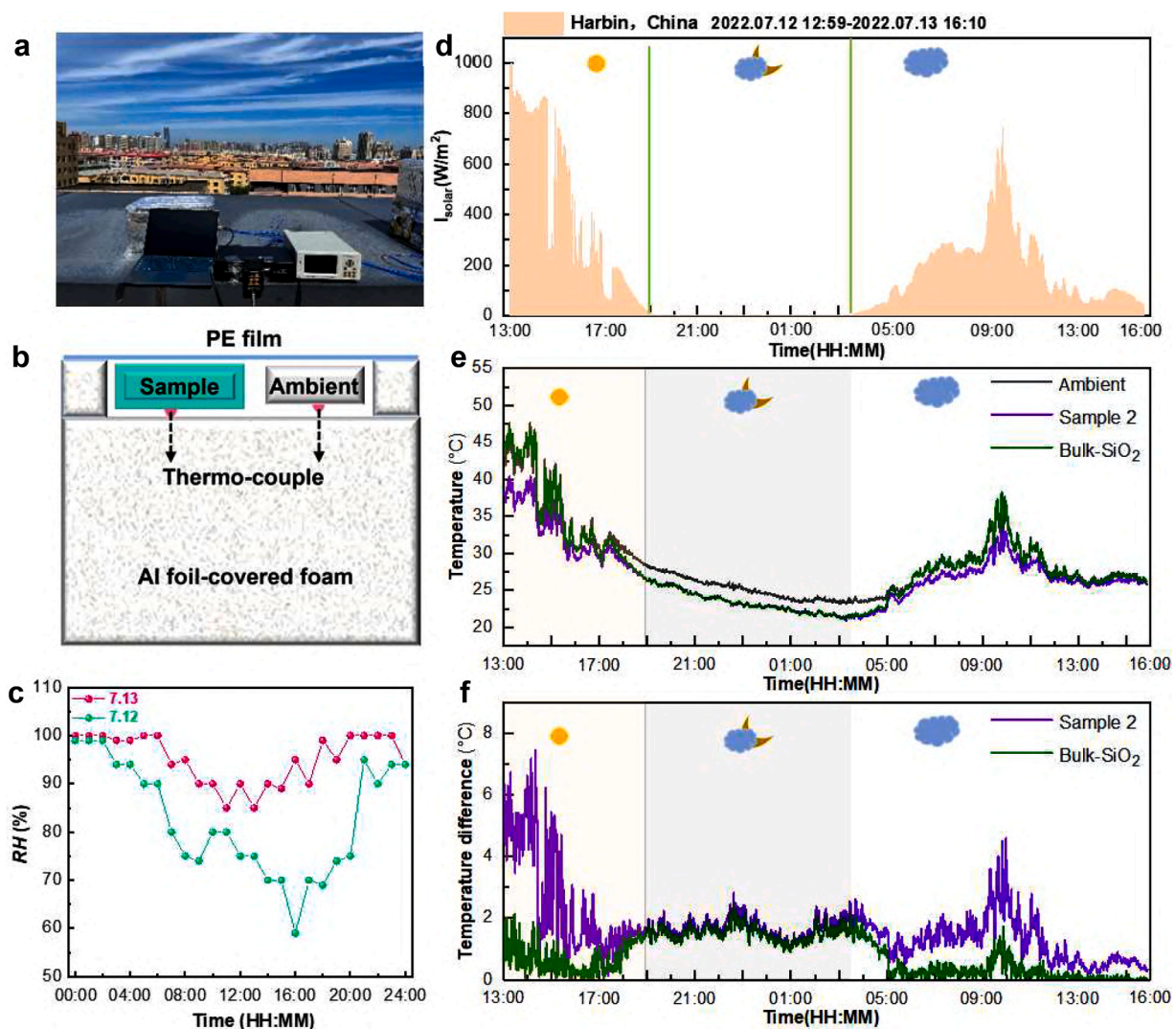
Fig. 5. Outdoor radiative cooling measurement of sample 2 and bulk SiO$_2$ in Harbin, China from July 12 to July 13. (a) Photo of outdoor test equipment. (b) Schematic of the outdoor measurement setup. A T-type thermocouple is applied to the back of the sample to measure its temperature. For ambient temperature monitoring, the T-type thermocouple is placed under a foam groove to avoid direct sunlight (ensuring air circulation). (c) Relative humidity (*RH*) during the test period (00:00–24: 00). (d) Solar irradiance I_{solar} during the test period. (e) Temperature profiles and (f) corresponding temperature drop (ΔT).

showing an average intensity of 843.1 W m^{-2} at noon during the first day (Fig. 5d). Under clear weather conditions (July 12th), sample 2 achieved an average ΔT of 5.5°C and a maximum ΔT of 7.9°C, compared to an average ΔT of 2.5°C and maximum ΔT of 5.3°C under cloudy weather (July 13th) (Fig. 5e and f). In comparison, the bulk SiO$_2$ sample shows almost no cooling capability during daytime hours. Under clear and low-humidity (*RH* below 50% throughout the hours, May 23, 2022) weather conditions, additional tests were conducted, which revealed an average 8°C temperature drop during the day (Fig. S10). The above results show that sample 2 exhibits significant cooling capacity under clear and moderate humidity conditions, and comparably good performance under cloudy and humid conditions (RH > 80 %), in line with other similar broadband emitters.

As shown in the past years for several radiative cooling materials [39,40], hydrophobic surface properties are desirable to increase their practical applicability, for instance by facilitating the removal of dust and other fine particulate via the action of rain or by actively washing the material, but also to help prevent the formation of mold which could severely limit the cooling efficiency. The self-cleaning behavior of the cooling films is a desirable property considering its outdoor applications [41–43]. Compared to the bulk SiO$_2$ sample, sample 2 exhibits a remarkable hydrophobicity with a contact angle (CA) of 131° (Fig. 6a).

High CA was observed for various fluids, including cola, milk, and ink (Fig. 6b–d). A wettability test (Movie 2) performed with deionized water shows that the micropillar structure allow water to easily roll off the sample at a tilting angle of 35°. This property facilitates the self-cleaning of the material, as further shown in Supplementary Movies S3 and S4 against contamination from soil and even rhodamine B dye, which are both easily washed away from sample 2, leading only to minor changes of its spectral response even after ten consecutive contamination/self-cleaning cycles (Fig. S11). This effect is attributed to the hydrophobic surface of the sample, which is due to its microstructure, as well as to the presence of F and C elements, as determined by EDS analysis (Fig. S12). Previous studies have suggested the formation of F/C compounds [44,45] following the etching treatment, which may typically form a thin film with a typical thickness of around 1 nm or less. At such vanishing thickness values, the possible presence of these compounds has no effect on the emissivity of the final sample. In addition, the high-resolution XPS spectra reveal the presence of the C1s peak in sample 2. As shown in Fig. 6e, sample 2 exhibits higher concentrations of -CF$_2$-, -CF-, and -C-CF$_x$ with binding energies of 293.4, 291.4, and 288.7 eV, respectively. The XPS peaks of other related elements (F1s, O1s, and Si2p) are shown in Fig. S13. The peaks at 688.3 and 685.8 eV are attributed to C-F$_x$ and C-F functional groups, respectively. The
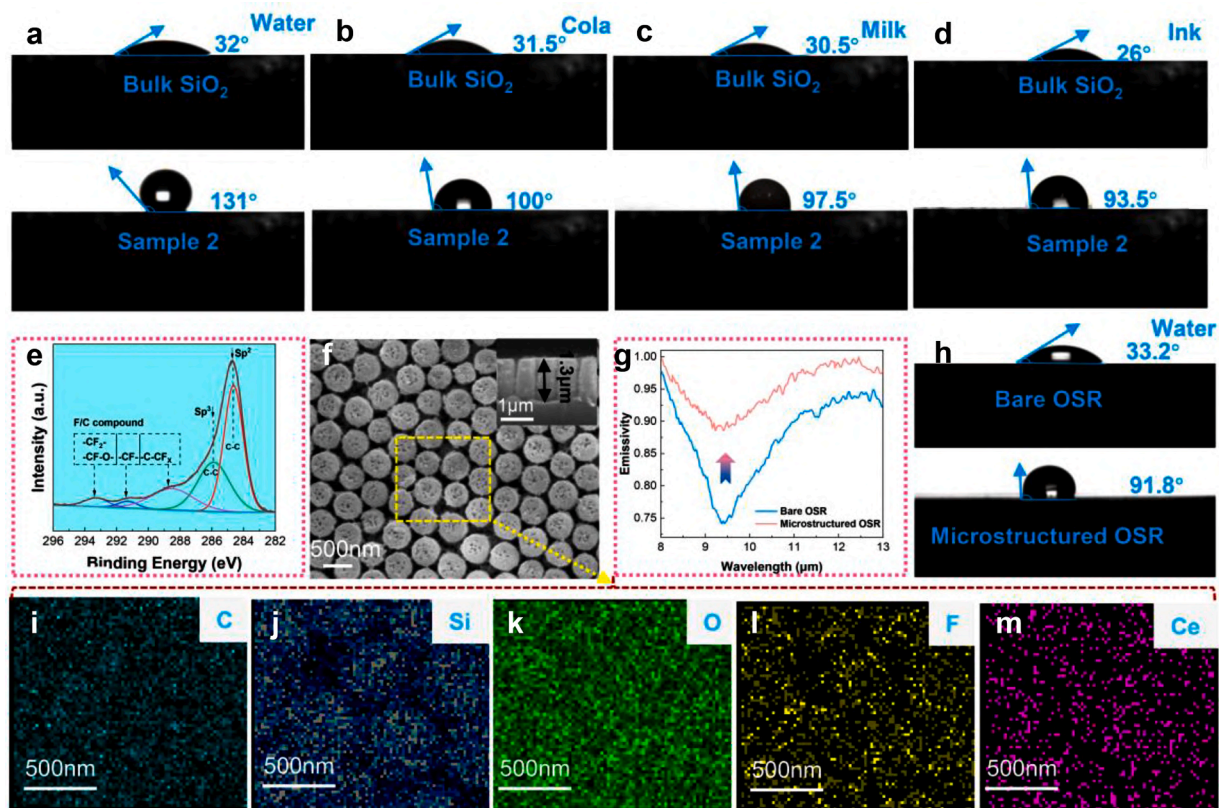
Fig. 6. The contact angles exhibited by bulk SiO_2 and sample 2 when in contact with different liquids: (a) Water; (b) Cola; (c) Milk; (d) Ink. (e) XPS spectra of C1s of sample 2. (f) SEM images of planes and cross sections for microstructured OSR. (g) The measured emissivity of the bare OSR and microstructured OSR in 8–13 μm. (h) The contact angles of the bare and microstructured OSR. The Energy disperses spectroscopy (EDS) elemental mapping of microstructured OSR: (i) C, (j) Si, (k) O, (l) F, (m) Ce.

results provide further evidence for the formation of F/C compounds. To verify the compatibility of the constructed submicron structures, similar micropillar arrays were fabricated on the surface of OSR. SEM images in Fig. 6f show the microstructured OSR with a micropillar array of approximately 1.3 μm. The infrared emissivity of the microstructured OSR at 8–13 μm increases from 0.87 to 0.95 compared to the bare OSR, as shown in Fig. 6g. Additionally, the microstructured OSR exhibits a CA of 91.8° compared to 33.2° observed for the bare OSR (Fig. 6h). Fig. 6 (i–m) display the energy-dispersive spectroscopy (EDS) elemental mapping images of C, Si, O, F, and Ce, which provide further evidence of the formation of F/C compounds on the surface of OSR. This further implies that the OSR sheet is composed of Ce-doped SiO_2, which explains why the etched OSR surface differs slightly from the etched SiO_2 surface. These findings confirm the validity of this compatible sub-micropatterning process to improve the emissivity and hydrophobicity of commercial OSRs.

4. Conclusion

A micropatterned SiO_2 radiative cooler was fabricated by RIE technology based on numerical and experimental optimization of its emissivity in the wavelength range of 8–13 μm. Optimized ranges were determined for the height, diameter, and spacing of the micropillars, which are compatible with reactive ion etching of a self-assembled mask of microspheres. The resulting samples showed a thermal emissivity of 0.94 in the wavelength range of 8–13 μm, with a 0.15 increase compared to the value of bulk SiO_2. When placed outdoors, the designed radiative cooler can passively reduce its temperature by an average of 5.5 °C during a clear day (at an average irradiance of 843.1 W m^{-2}), compared to the surrounding air temperature. Moreover, similar micropillar arrays constructed on the surface of OSR demonstrated substantial

improvements in emissivity and hydrophobicity. The proposed approach for designing and fabricating submicron patterns presents a promising opportunity for improving the characteristics of SiO_2 layers while avoiding the drawbacks of previous techniques, such as high costs and limited compatibility.

CRediT authorship contribution statement

Zhenmin Ding: Investigation, Writing – original draft, Visualization, Methodology. **Xin Li:** Investigation, Writing – review & editing. **Hulin Zhang:** Methodology. **Dukang Yan:** Formal analysis. **Jérémy Werlé:** Validation, Methodology, Formal analysis, Data curation. **Ying Song:** Writing – review & editing. **Lorenzo Pattelli:** Conceptualization, Data curation, Writing – review & editing, Supervision, Resources, Funding acquisition. **Jiupeng Zhao:** Supervision, Project administration. **Hongbo Xu:** Conceptualization, Supervision, Funding acquisition, Resources. **Yao Li:** Funding acquisition, Conceptualization, Resources.

Declaration of Competing Interest

The authors declare that they have no known competing financial interests or personal relationships that could have appeared to influence the work reported in this paper.

Data availability

Numerical models and simulation data relative to the optimization of the micropatterned emitter are available at https://zenodo.org/doi/10.5281/zenodo.10202117.

Acknowledgments

Supplementary materials

Supplementary material associated with this article can be found, in the online version, at doi:10.1016/j.ijheatmasstransfer.2023.125004.

References

[1] X. Yin, R. Yang, G. Tan, S. Fan, Terrestrial radiative cooling: Using the cold universe as a renewable and sustainable energy source, Science 370 (2020) 786–791.

[2] Z. Ding, X. Li, X. Fan, M. Xu, J. Zhao, Y. Li, H. Xu, A Review of the development of colored radiative cooling surfaces, Carbon Capture Sci. Technol. 4 (2022), 100066.

[3] J. Chen, L. Lu, Q. Gong, A new study on passive radiative sky cooling resource maps of China, Energ. Convers. Manag. 237 (2021), 114132.

[4] X. Yu, J. Chan, C. Chen, Review of radiative cooling materials: performance evaluation and design approaches, Nano Energy 88 (2021), 106259.

[5] D. Zhao, A. Aili, Y. Zhai, S. Xu, G. Tan, X. Yin, R. Yang, Radiative sky cooling: Fundamental principles, materials, and applications, Appl. Phys. Rev. 6 (2019), 021306.

[6] U. Sajjad, K. Hamid b, T. Rehman, M. Sultan, N. Abbas, H. Ali, M. Imran, M. Muneeshwaran, J. Chang, C. Wang, Personal thermal management - a review on strategies, progress, and prospects, Int. Commun. Heat Mass 130 (2022), 105739.

[7] L. Chen, K. Zhang, M. Ma, S. Tang, F. Li, X. Niu, Sub-ambient radiative cooling and its application in buildings, Build Simul. 13 (2020) 1165–1189.

[8] G. Ulpiani, G. Ranzi, K. Shah, J. Feng, M. Santamouris, On the energy modulation of daytime radiative coolers: a review on infrared emissivity dynamic switch against overcooling, Sol. Energy 209 (2020) 278–301.

[9] X. Li, Z. Ding, L. Kong, X. Fan, Y. Li, J. Zhao, L. Pan, D.S. Wiersma, L. Pattelli, H. Xu, Recent progress in organic-based radiative cooling materials: fabrication methods and thermal management properties, Mater. Adv. 4 (2023) 804–822.

[10] X. Zhao, H. Xie, H. Liu, L. Wang, Y. Qu, S.C. Li, S. Liu, A.H. Brozena, Z. Yu, J. Srebric, L. Hu, A solution-processed radiative cooling glass, Science 382 (2023) 684–691.

[11] M.T. Tsai, S.W. Chang, Y.J. Chen, H.L. Chen, P.H. Lan, D.C. Chen, F.H. Ko, Y.C. Lo, H.C. Wang, D. Wan, Scalable, flame-resistant, superhydrophobic ceramic metafibers for sustainable all-day radiative cooling, Nano Today 48 (2023), 101745.

[12] N.D. Tyrrell, A proposal that would ban manufacture, supply, and use of all fluoropolymers and most fluorinated reagents within the entire EU, Org. Process Res. Dev. 27 (2023) 1422–1426.

[13] C. Sonne, B.M. Jenssen, J. Rinklebe, S.S. Lam, M. Hansen, R. Bossi, K. Gustavson, R. Dietz, EU need to protect its environment from toxic per- and polyfluoroalkyl substances, Sci. Total Environ. 876 (2023), 162770.

[14] L. Prasittisopin, W. Ferdous, V. Kamchoom, Microplastics in construction and built environment, Dev. Built Environ. 15 (2023), 100188.

[15] D. Chae, M. Kim, P.H. Jung, S. Son, J. Seo, Y. Liu, B.J. Lee, H. Lee, Spectrally selective inorganic-based multilayer emitter for daytime radiative cooling, ACS Appl. Mater. Int. 12 (2020) 8073–8081.

[16] H. Ma, K. Yao, S. Dou, M. Xiao, M. Dai, L. Wang, H. Zhao, J. Zhao, Y. Li, Y. Zhan, Multilayered SiO_2/Si_3N_4 photonic emitter to achieve high-performance all-day radiative cooling, Sol. Energy Mater. Sol. C 212 (2020), 110584.

[17] Y. Dai, Z. Zhang, C. Ma, Radiative cooling with multilayered periodic grating under sunlight, Opt. Commun. 475 (2020), 126231.

[18] X. Zhang, W. Yang, Z. Shao, Y. Li, Y. Su, Q. Zhang, C. Hou, H. Wang, A moisture-wicking passive radiative cooling hierarchical metafabric, ACS Nano 16 (2022) 2188–2197.

[19] X. Wang, X. Liu, Z. Li, H. Zhang, Z. Yang, H. Zhou, T. Fan, Scalable flexible hybrid membranes with photonic structures for daytime radiative cooling, Adv. Funct. Mater. 30 (2020), 1907562.

[20] C. Lin, Y. Li, C. Chi, Y. Kwon, J. Huang, Z. Wu, J. Zheng, G. Liu, C. Tso, C. Chao, B. Huang, A solution-processed inorganic emitter with high spectral selectivity for efficient subambient radiative cooling in hot humid climates, Adv. Mater. 34 (2022), 2109350.

[21] L. Liu, X. Shan, X. Hu, W. Lv, J. Wang, Superhydrophobic silica aerogels and their layer-by-layer structure for thermal management in harsh cold and hot environments, ACS Nano 15 (2021) 19771–19782.

[22] Y. Lu, Z. Chen, L. Ai, X. Zhang, J. Zhang, J. Li, W. Wang, R. Tan, N. Dai, W. Song, A universal route to realize radiative cooling and light management in photovoltaic modules, Sol. RRL 1 (2017), 1700084.

[23] M. Salary, H. Mosallaei, Photonic metasurfaces as relativistic light sails for doppler-broadened stable beam-riding and radiative cooling, Laser Photonics Rev. 14 (2020), 1900311.

[24] D. Wu, C. Liu, Z. Xu, Y. Liu, Z. Yu, L. Yu, L. Chen, R. Li, R. Ma, H. Ye, The design of ultra-broadband selective near-perfect absorber based on photonic structures to achieve near-ideal daytime radiative cooling, Mater. Des. 139 (2018) 104–111.

[25] M. Tsai, T. Chuang, C. Meng, Y. Chang, S. Lee, High performance midinfrared narrow-band plasmonic thermal emitter, Appl. Phys. Lett. 89 (2006), 173116.

[26] A. Raman, M. Anoma, L. Zhu, E. Rephaeli, S. Fan, Passive radiative cooling below ambient air temperature under direct sunlight, Nature 515 (2014) 540–544.

[27] Y. Zhai, Y. Ma, S.N. David, D. Zhao, R. Lou, G. Tan, R. Yang, X. Yin, Scalable-manufactured randomized glass-polymer hybrid metamaterial for daytime radiative cooling, Science 355 (2017) 1062–1066.

[28] G. Whitworth, J. Jaramillo-Fernandez, J. Pariente, P. Garcia, A. Blanco, C. Lopez, C. Sotomayor-Torres, Simulations of micro-sphere/shell 2D silica photonic crystals for radiative cooling, Opt. Express 29 (2021) 16857–16866.

[29] L. Zhu, A.P. Raman, S. Fan, Radiative cooling of solar absorbers using a visibly transparent photonic crystal thermal blackbody, Proc. Natl. Acad. Sci. U. S. A. 112 (2015) 12282–12287.

[30] B. Zhao, K. Lu, M. Hu, J. Liu, L. Wu, C. Xu, Q. Xuan, G. Pei, Radiative cooling of solar cells with micro-grating photonic cooler, Renew. Energy 191 (2022) 662e668.

[31] Z. Ding, L. Pattelli, H. Xu, W. Sun, X. Li, L. Pan, J. Zhao, C. Wang, X. Zhang, Y. Song, J. Qiu, Y. Li, R. Yang, Iridescent daytime radiative cooling with no absorption peaks in the visible range, Small (2022), 2202400.

[32] Z. Wang, Y. Wei, Z. Liu, G. Duan, D. Yang, P. Cheng, Perfect solar absorber with extremely low infrared emissivity, Photonics 9 (2022) 574.

[33] Y. Nishijima, S. Morimoto, A. Balčytis, T. Hashizume, R. Matsubara, A. Kubono, N. To, M. Ryu, J. Morikawa, S. Juodkazis, Coupling of molecular vibration and metasurface modes for efficient mid-infrared emission, J. Mater. Chem. C 10 (2022) 451–462.

[34] C. Granqvist, A. Hjortsberg, Radiative cooling to low temperatures: General considerations and application to selectively emitting SiO films, J. Appl. Phys. 52 (1981) 4205–4220.

[35] A. Berk, G.P. Anderson, P.K. Acharya, L.S. Bernstein, L. Muratov, J. Lee, M. Fox, S. M. Adler-Golden, J.H. Chetwynd, M.L. Hoke, R.B. Lockwood, J.A. Gardner, T.W. Cooley, Modtran5: 2006 update, in algorithms and technologies for multispectral, hyperspectral, and ultraspectral imagery XII. 6233, 62331F-62331F-8.

[36] H. Hogstrom, G. Forssell, C. Ribbing, Realization of selective low emittance in both thermal atmospheric windows, Opt. Eng. 44 (2005), 026001.

[37] Z. Wang, H. Ding, D. Liu, C. Xu, B. Li, S. Niu, L. Ren, Large-scale bio-inspired flexible antireflective film with scale-insensitivity arrays, ACS Appl. Mater. Interfaces 13 (2021) 23103–23112.

[38] J. Huang, C. Lin, Y. Li, B. Huang, Effects of humidity, aerosol, and cloud on sub-ambient radiative cooling, Int. Commun. Heat Mass 186 (2022), 122438.

[39] J. Liu, W. Ma, X. Deng, H. Cai, Superhydrophobic nanoparticle mixture coating for highly efficient all-day radiative cooling, Appl. Therm. Eng. 228 (2023), 120490.

[40] Y. Sun, H. He, X. Huang, Z. Guo, Superhydrophobic SiO_2-glass bubbles composite coating for stable and highly efficient daytime radiative cooling, ACS Appl. Mater. Interfaces 15 (2023) 4799–4813.

[41] H. Wang, C. Xue, X. Guo, B. Liu, Z. Ji, M. Huang, S. Jia, Superhydrophobic porous film for daytime radiative cooling, Appl. Mater. Today 24 (2021), 101100.

[42] S. Wang, Y. Wang, Y. Zou, G. Chen, J. Ouyang, D. Jia, Y. Zhou, Biologically inspired scalable-manufactured dual-layer coating with a hierarchical micropattern for highly efficient passive radiative cooling and robust superhydrophobicity, ACS Appl. Mater. Interfaces 13 (2021) 21888–21897.

[43] F. Chen, Q. Tian, T. Wang, L. Ma, R. Liu, S. Wang, Fabrication of a multifunctional antibacterial Cotton-based fabric for personal cooling, Appl. Surf. Sci. 609 (2023), 155291.

[44] Y. Pai, G. Lin, Nano-roughened teflon-like film coated polyethylene terephthalate substrate with trifluoromethane plasma enhanced hydrophobicity and transparency, J. Electrochem. Soc. 158 (2011) G173–G177.

[45] S. You, Y.J. Lee, H. Chae, C. Kim, Plasma etching of SiO_2 contact holes using hexafluoroisopropanol and C_4F_8, Coatings 12 (2022) 679.